

Survival in the Neptune desert: LTT 9779 b kept its atmosphere thanks to an unusually X-ray faint host star

Jorge Fernández Fernández,^{1,2}★ Peter J. Wheatley^{1,2}† George W. King^{3,1,2} James S. Jenkins^{4,5}

¹*Department of Physics, University of Warwick, Gibbet Hill Road, Coventry CV4 7AL, UK*

²*Centre for Exoplanets and Habitability, University of Warwick, Gibbet Hill Road, Coventry CV4 7AL, UK*

³*Department of Astronomy, University of Michigan, Ann Arbor, MI 48109, USA*

⁴*Instituto de Estudios Astrofísicos, Facultad de Ingeniería y Ciencias, Universidad Diego Portales, Av. Ejército 441, Santiago, Chile*

⁵*Centro de Astrofísica y Tecnologías Afines (CATA), Casilla 36-D, Santiago, Chile*

Accepted XXX. Received YYY; in original form ZZZ

ABSTRACT

The Neptunian desert is a region in period-radius parameter space with very few Neptune-sized planets at short orbital periods. Amongst these, LTT 9779 b is the only known Neptune with a period shorter than one day to retain a significant H-He atmosphere. If the Neptune desert is the result of X-ray/EUV-driven photoevaporation, it is surprising that the atmosphere of LTT 9779 b survived the intense bombardment of high energy photons from its young host star. However, the star has low measured rotational broadening, which points to the possibility of an anomalously slow spin period and hence a faint X-ray emission history that may have failed to evaporate the planet’s atmosphere. We observed LTT 9779 with XMM-Newton and measured an upper limit for its X-ray luminosity that is a factor of fifteen lower than expected for its age. We also simulated the evaporation past of LTT 9779 b and found that the survival of its atmosphere to the present day is consistent with an unusually faint XUV irradiation history that matches both the X-ray and rotation velocity measurements. We conclude that the anomalously low X-ray irradiation of the one Neptune seen to survive in Neptunian desert supports the interpretation of the desert as primarily a result of photoevaporation.

Key words: stars: individual: LTT 9779 – stars: activity – X-rays: stars – planets & satellites: atmospheres – planet-star interactions

1 INTRODUCTION

The Kepler space telescope uncovered thousands of exoplanets during its 9 years of operation, many of them without an analogue in our Solar System. This included super-Earths and sub-Neptunes in tightly packed systems (Borucki et al. 2011).

These discoveries have revealed a scarcity of Neptune to Saturn sized planets (3–10 R_E) at short orbital periods of < 3 days. This region, known as the sub-Jovian or Neptunian desert, has become more statistically significant with further planet discoveries by the K2 and TESS missions (e.g. Szabó & Kiss 2011; Benítez-Llambay et al. 2011; Sanchis-Ojeda et al. 2014; Mazeh et al. 2016).

Since close-in planets are easier to detect in transit surveys, with many detections of hot Jupiters and even Earth-sized worlds with periods under two days (Murray-Clay et al. 2009; Mazeh et al. 2016), the Neptunian desert cannot be explained as an observational bias alone, and must be caused by underlying physical mechanisms affecting these planets during their formation and/or evolution.

The origin of the Neptunian desert has been attributed to the inability of planets in this region to hold onto their gaseous envelopes due to atmospheric escape (Kurokawa & Kaltenecker 2013; Kurokawa & Nakamoto 2014; Ionov et al. 2018; Owen & Lai 2018), a phe-

nomenon that is also thought to give rise to the period-radius valley (Lopez et al. 2012; Owen & Wu 2013; Fulton et al. 2017; Owen & Wu 2017).

Neptune-sized planets that formed in the desert, or migrated there in their youth, would be stripped of their H/He envelopes joining the more abundant population of hot rocky worlds with smaller radii. Hot Jupiters (>10 R_E), on the other hand, are thought to be stable against atmospheric loss thanks to their deep gravitational potentials (Yelle 2004; Murray-Clay et al. 2009; Vissapragada et al. 2022). The underlying mechanisms that drive atmospheric escape, however, are still unclear, and several have been proposed.

One such mechanism, photoevaporation, derives the energy for atmospheric escape from the X-ray and extreme ultraviolet radiation (together, XUV) originating in the host star’s corona. These high energy photons are readily absorbed by the upper layers of large H/He-rich atmospheres, heating and expanding the gas, and driving a hydrodynamic wind that escapes the planet (Lecavelier Des Etangs 2007; Owen & Wu 2013; Lopez & Fortney 2014).

Owen & Lai (2018) argued that two separate mechanisms are responsible for the formation of the two boundaries of the Neptune desert. Its lower boundary is sculpted by the photoevaporation of the atmospheres of Neptune-sized planets. The upper boundary of the desert, over which hot Jupiters lie, is the result of a tidal disruption barrier that interrupts the high-eccentricity migration of gas giants.

Alternatively, it has been suggested the Neptunian desert may arise

★ E-mail: jorge.fernandez-fernandez@warwick.ac.uk

† E-mail: p.j.wheatley@warwick.ac.uk

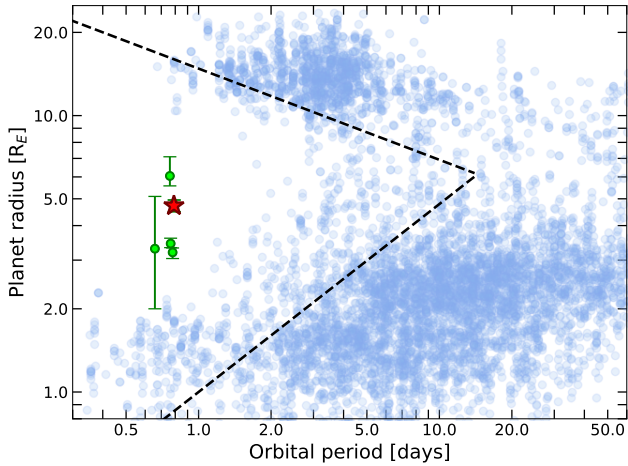


Figure 1. Plot of orbital period against planet radius, with LTT 9779 b marked as a red star. The upper and lower bounds of the Neptune desert are shown as black dashed lines, following [Mazeh et al. \(2016\)](#). Data points represent confirmed exoplanets source from the NASA *Exoplanet Archive*, with ultra-short period Neptunes shown as green circles.

due to the effects of Roche Lobe Overflow (RLO) on hot Neptunes ([Jackson et al. 2017](#); [Koskinen et al. 2022](#)), or as a result of high-eccentricity migration ([Matsakos & Königl 2016](#)).

In Figure 1 we plot all validated exoplanets from the NASA *Exoplanet Archive*¹ as of July 2023. The Neptune desert is delimited by the boundaries proposed by [Mazeh et al. \(2016\)](#), who defined the lower and upper edges by finding the boundaries of maximum contrast of planet number density.

In the past few years, a handful of ultra-short period Neptunes have been discovered, a group of planets distinct from the larger exoplanet population, plotted as green points on Figure 1. Some of these ultra-short period Neptunes are consistent with a rocky density and hence a high-mass core (TOI-849 b, [Armstrong et al. \(2020\)](#); TOI-332 b, [Osborn et al. \(2023\)](#)) and whose origins are still unknown; others lack mass measurements (K2-399 b, [Christiansen et al. 2022](#)) or the necessary precision in mass measurement to constrain their densities and internal structures (K2-266 b, [Rodríguez et al. 2018](#)). There is also a growing population of low density sub-Neptunes in the desert at periods of 1–3 days, such as NGTS-4 b ([West et al. 2019](#)) and GJ 1214 b ([Cloutier et al. 2021](#)).

Finally, LTT 9779 b (marked in red on Fig. 1) is a hot Neptune in an extremely short orbit around a G7V star with a period of just 0.79 days (about 19 hours, [Jenkins et al. 2020](#)). Its measured mass ($29.30^{+0.78}_{-0.81} M_{\oplus}$) and radius ($4.72 \pm 0.23 R_{\oplus}$) require a very low density ($1.53 \pm 0.23 \text{ g cm}^{-3}$) characteristic of a volatile-rich planet.

The presence of a large gaseous atmosphere has been confirmed by [Crossfield et al. \(2020\)](#) and [Dragomir et al. \(2020\)](#) with infrared observations from Spitzer, [Edwards et al. \(2023\)](#) with HST/WFC3 transmission spectroscopy, and by [Hoyer et al. \(2023\)](#) with CHEOPS occultation measurements. The existence of a substantial H/He-rich atmosphere makes LTT 9779 b a one-of-a-kind planet and its survival deep in the Neptune desert puzzling. If the Neptune desert is the result of X-ray driven evaporation, one would expect that a highly irradiated

Table 1. Stellar parameters of LTT 9779.

Parameter	Units	Value	Reference
Astrometric			
RA (J2000)	hh:mm:ss	23 : 54 : 40.21	Gaia DR3 ^c
Dec (J2000)	dd:mm:ss	−37 : 37 : 40.52	Gaia DR3 ^c
μ_{RA}	mas yr ^{−1}	247.634 ± 0.013	Gaia DR3 ^c
μ_{Dec}	mas yr ^{−1}	$−69.752 \pm 0.014$	Gaia DR3 ^c
Parallax	mas	12.338 ± 0.017	Gaia DR3 ^c
Distance	pc	81.050 ± 0.011	Gaia DR3 ^c
Physical			
Spectral type	—	G7V	J20 ^a
V	mag	9.76 ± 0.03	UCAC4 ^b
T_{eff}	K	5480 ± 42	J20 ^a
M_{\star}	M_{\odot}	$1.02^{+0.02}_{-0.03}$	J20 ^a
R_{\star}	R_{\odot}	0.949 ± 0.006	J20 ^a
L_{\star}	L_{\odot}	0.708 ± 0.016	J20 ^a
[Fe/H]	dex	0.25 ± 0.04	J20 ^a
$v \sin i$	km s ^{−1}	1.06 ± 0.37	J20 ^a
P_{rot}	days	< 45	J20 ^a
Age	Gyr	$2.0^{+1.3}_{-0.9}$	J20 ^a
$\log R'_{\text{HK}}$	dex	$−5.10 \pm 0.04$	J20 ^a

^a J20: [Jenkins et al. \(2020\)](#)

^b UCAC4: [Zacharias et al. \(2012\)](#)

^c Gaia DR3: [Gaia Collaboration et al. \(2022\)](#)

^d 2MASS: [Cutri et al. \(2003\)](#)

Neptune-sized planet, such as LTT 9779 b, should have already been stripped of its envelope.

We list the stellar parameters of LTT 9779 in Table 1 and note that the star has very low measured rotational broadening ($v \sin i$). Assuming the rotation axis of the star is not pointing towards the Earth, this implies a spin period of around 45 d, which is unusually long for a star of its type and age ([Johnstone et al. 2021](#)). Since stellar activity and X-ray emission are strongly correlated with spin period (e.g [Wright et al. 2011](#)) the slow spin of LTT 9779 suggests diminished XUV emission that might have failed to remove the planet’s atmosphere.

In this paper, we test this scenario for the survival of LTT 9779 b. We observed LTT 9779 with *XMM-Newton* and placed a limit on its X-ray luminosity (Sect. 2). We then modelled the rotation and X-ray emission history of the star (Sect. 3) and the possible evaporation histories of LTT 9779 b (Sects. 4 & 5). In Sect. 6, we conclude that the survival of LTT 9779 b in the Neptunian can indeed be explained by an unusually low X-ray emission history of its host star, adding weight to the suggestion that the wider Neptunian desert originates from photoevaporation.

2 X-RAY OBSERVATIONS & ANALYSIS

LTT 9779 was observed with the *XMM-Newton* spacecraft on May 27th and 28th 2021 for a continuous exposure of 52 ks (ObsID: 0884250101, PI: Wheatley). The star, however, was not detected in the standard pipeline outputs. We inspected the data from the the EPIC pn ([Strüder et al. 2001](#)) and MOS ([Turner et al. 2001](#)) detectors using the proper-motion corrected coordinates of the star on the pipeline-processed event list, adopting both wide and narrow standard energy bands. Nevertheless, we found no evidence of a detection of our target.

We also found that the particle background in the detectors increased significantly towards the end of the observation, and hence we decided to remove these noisy sections by dropping the time in-

¹ The NASA *Exoplanet Archive* can be accessed at <https://exoplanetarchive.ipac.caltech.edu/>.

Table 2. Upper limit count rates for the PN and MOS1+2 instruments.

Instrument	Energy range keV	Exposure ks	Source counts	Expected background counts	90% upper limit source counts	Upper limit rate counts ks ⁻¹
pn	0.15 – 2.0	31.7	91	69.6	37.3	1.177
MOS1+2	0.20 – 2.0	42.3	32	34.3	9.64	0.228

Table 3. Upper limit X-ray fluxes and luminosities predicted by the APEC model from pn and MOS count rates.

Energy range (keV)	Instrument	X-ray flux (10 ⁻¹⁵ erg cm ⁻² s ⁻¹)	Luminosity (10 ²⁷ erg s ⁻¹)
0.1 – 2.4	pn	2.87	2.26
	MOS1+2	2.83	2.23
0.2 – 2.4	pn	2.07	1.63
	MOS1+2	2.04	1.60

tervals with count rates higher than 0.5 s⁻¹ for pn and 0.35 s⁻¹ for MOS in the band 10–12 keV across the full area of the detector. The remaining data amounted to 31.7 ks for pn and 42.3 ks for each MOS. The target star, however, remained undetected after this removal of noisy data.

In the absence of a detection, we estimated an upper limit X-ray flux from LTT 9779 using the method described by Farihi et al. (2018). This analysis is also based on the standard data analysis threads using the XMM Science Analysis Software (SAS)² version 19.

We first applied an extraction area around the proper motion corrected coordinates of the source with a circular aperture of radius 16 arcseconds, as well as a secondary aperture of radius 80 arcseconds for the background in a nearby region that contained no X-ray sources. We collected the detected counts in these regions using the energy ranges 0.15 – 2.0 keV for pn and 0.2 – 2.0 keV for MOS. We discarded counts over 2 keV as coronal emission from stellar activity is relatively soft (Güdel 2004). We then scaled the background counts to the aperture area used for the source region. In the case of the two MOS detectors, we combined the count rates from both instruments by making use of common Good Time Intervals (GTI) and adding up the detected counts.

We then applied the method by Kraft et al. (1991) to estimate 90% confidence upper limit count rates. They model noise using a Poisson distribution and adopt a Bayesian approach with the prior that the source count rate cannot be negative. The results, shown in Table 2, indicate upper limit count rates of 1.18 ks⁻¹ for pn and 0.23 ks⁻¹ for the combined MOS1 and MOS2 detectors (hereafter MOS1+2).

In order to convert the count rates to X-ray fluxes, we built model spectra using the software XSPEC version 12.12.1 (Arnaud 1996), which we then scaled to match the upper limit count rates in Table 2. In the case of MOS, we loaded the response and ancillary files for MOS1 only, and scaled the model to half the combined MOS1+2 count rate. We adopted solar abundances from Asplund et al. (2009) and accounted for interstellar absorption with the TBABS model by Wilms et al. (2000). We estimated an interstellar hydrogen column density of 2.5 × 10¹⁹ cm⁻² following Redfield & Linsky (2001), who determined a hydrogen density of 0.1 cm⁻³ for the local interstellar medium. We used a single-temperature APEC model to simulate the spectrum (Smith et al. 2001), which models the emission spectrum of collisionally-ionized diffuse gas. In order to deter-

mine a plasma temperature for our spectral model, we adopted the luminosity-temperature relation by Güdel (2004), which shows that average coronal temperatures increase with X-ray luminosity on Sun-like stars. We found that their relation is consistent with our choice of model for plasma temperatures between 0.15 and 0.3 keV. For our upper limit calculation we selected a temperature of 0.15 keV, since this results in the most conservative (higher) limit.

Finally, we scaled and integrated the spectral model, and estimated X-ray fluxes and luminosities for both the pn and MOS1+2 instruments, as shown on Table 3. The pn and MOS limits are very similar, corresponding to upper limit X-ray luminosities of 2.2 × 10²⁷ erg s⁻¹ in the 0.1–2.4 keV energy range, and 1.6 × 10²⁷ erg s⁻¹ in the 0.2–2.4 keV band.

The measured rotational velocity $v \sin i$ of LTT 9779 implies a spin period of 45 d, assuming its spin axis is aligned with the planet’s orbit. Using rotation-activity relations (e.g. Wright et al. 2011), we estimated an X-ray luminosity of 3.9 × 10²⁷ erg s⁻¹ in the band 0.1–2.4 keV, which is within a factor of two of our upper limit – consistent with the 1 σ uncertainty on the measured $v \sin i$.

We also verified that the exact value for the hydrogen column density did not have a strong effect on the spectral model for values of $N_H \leq 10^{21}$ cm⁻². A change of a factor of two in this quantity resulted in only a difference of a few percent in the output fluxes.

3 STELLAR ROTATION AND XUV HISTORY

In order to model the XUV emission history of LTT 9779, we adopted the rotation evolution models by Johnstone et al. (2021). Those authors model the spin evolution of stars of different masses by combining angular momentum transfer mechanisms within the star (core-envelope coupling) as well as interactions with its environment (stellar wind and disc-locking), and constrain the distribution of stellar rotation rates to observations of clusters of ages 12 Myr to 2.5 Gyr. Their models predict that the average rotation period for Solar-mass star of 2 Gyr age, such as LTT 9779, is 14 days, with a 2 σ spread from 12 to 16 days. The spin and X-ray luminosity evolution of a 1M_⊙ star according to this model are shown in black in Figure 2, with the the X-ray emission determined from the spin evolution using rotation-activity relations (Pizzolato et al. 2003; Wright et al. 2011, 2018).

Even though the rotation period of LTT 9779 is unknown, Jenkins et al. (2020) were able to place an upper limit on the period of 45 days based on a HARPS $v \sin i$ of 1.06 ± 0.37 km s⁻¹. This 45 d period will correspond to the true rotation period of the star if its spin axis is aligned with the orbit of the planet (i.e. $i = 90^\circ$). The implied period remains well above 14 d for stellar inclinations greater than 20 deg, and the probability of an inclination of 20 deg or less is only 6%, even if the stellar inclination is randomly misaligned with the planet’s orbit. Furthermore, Jenkins et al. (2020) also measured the strength of the Ca II HK lines and found a log R'_{HK} value of -5.10 ± 0.04 dex, which is indicative of a very low activity and also supports the star having an unusually slow rotation period.

In order to model a plausible low XUV emission history, we choose to adopt the 45-day limit as the current rotation period of the star and

² Users Guide to the XMM-Newton Science Analysis System", Issue 17.0, 2022 (ESA: XMM-Newton SOC), <https://www.cosmos.esa.int/web/xmm-newton/sas-threads>

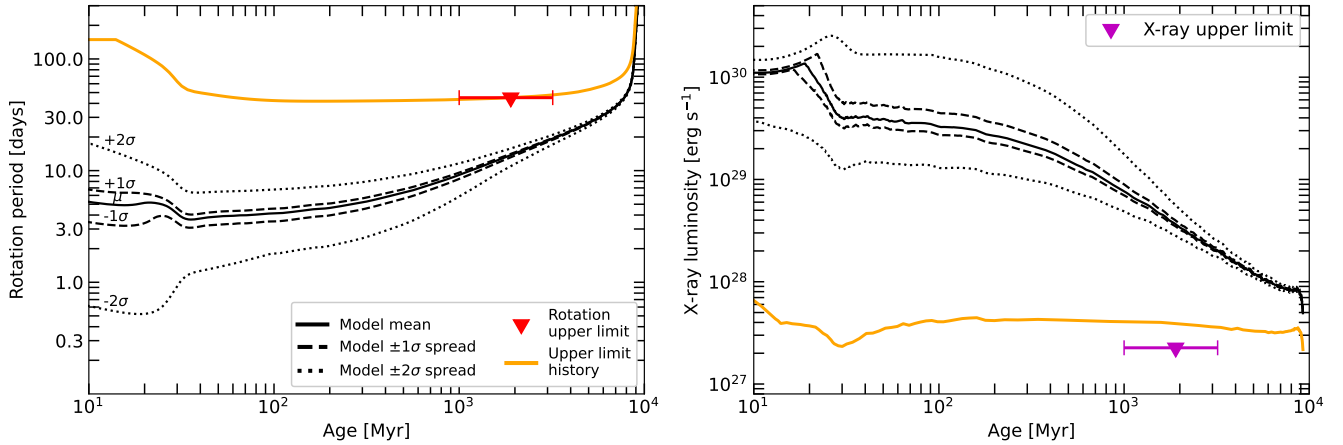


Figure 2. **Left panel:** spin histories for a $1 M_{\odot}$ star predicted by [Johnstone et al. \(2021\)](#), including the population mean, 1σ , and 2σ spreads, as well as the spin history fitted to the 45-day upper limit spin of LTT 9779. **Right panel:** X-ray emission histories in the 0.1–2.4 keV band corresponding to the spin histories on the left panel. Our X-ray upper limit measured from *XMM-Newton* observations is shown as a magenta triangle.

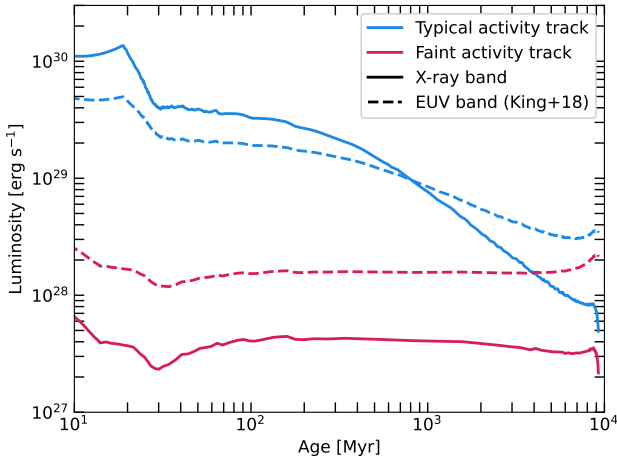


Figure 3. Emission histories for the X-ray band (solid lines) and EUV band (dashed lines) for the two stellar models discussed in Section 3: the predicted history for a solar mass star (blue) and the fainter history motivated by spin and X-ray measurements (red). The EUV band was estimated from the X-rays using the scaling law by [King et al. \(2018\)](#).

use the models by [Johnstone et al. \(2021\)](#) to extrapolate to earlier and later times. The spin and X-ray luminosity evolution in this scenario are shown in orange in Figure 2.

Our results for a typical star in Figure 2 show a predicted X-ray luminosity of $3.4 \times 10^{28} \text{ erg s}^{-1}$ for LTT 9779 at the present time, which is a factor of 15 brighter than our *XMM-Newton* upper limit from Sect. 2. In contrast, our X-ray upper limit is within a factor of 2 of the predicted X-ray luminosity for the 45 d spin period corresponding to the measured $v \sin i$ and an aligned system. Our *XMM-Newton* upper limit is clearly more consistent with the anomalously slow rotation scenario.

4 EVOLUTION MODELLING

We used the X-ray luminosity evolution for the different scenarios shown in Figure 2 to model the evaporation history of the LTT 9779 b

in order to determine the conditions under which the planetary atmosphere will be stripped.

We used the *photoevolver*³ code ([Fernández Fernández et al. 2023](#)), which combines three ingredients: (1) a description of the stellar X-ray history, using the model by [Johnstone et al. \(2021\)](#) described in Section 3, (2) the envelope structure model by [Chen & Rogers \(2016, Eqn. 5\)](#) based on MESA hydrodynamic simulations, which links the atmospheric mass to its size, and (3) the mass loss model by [Kubyshkina et al. \(2018\)](#), which translates incident X-ray irradiation into atmospheric mass loss rate.

At each simulation time step, the XUV flux incident on the planet is drawn from the stellar tracks in Figure 2 and then used to remove some mass from the atmosphere, calculated using the mass loss model. The envelope size is then recalculated with the new mass, and the age advances one time step forward. We evolved the planet from the age of 10 Myr, the time at which the protoplanetary disc has fully dissipated ([Fedele et al. 2010](#)) and any boil-off processes have completed ([Lammer et al. 2016; Owen & Wu 2016](#)), to 5 Gyr, with a fixed time step of 0.1 Myr. We considered the envelope stripped when its mass reached a value below 0.01% of the planet’s mass, as it is the lower limit for which the envelope model by [Chen & Rogers \(2016\)](#) is rated.

We adopted two spin period histories from Figure 2 to find feasible evaporation pasts for LTT 9779 b: one matching the typical spin period distribution for a solar-mass star, and another matching the star’s measured rotation upper limit of 45 days at its current age. We also estimated the extreme ultraviolet (EUV) stellar emission in the band 0.0136–0.1 keV using the empirical relations by [King et al. \(2018\)](#), which are based on Solar *TIMED/SEE* data. We plot the relative contributions of the X-ray and EUV bands on Figure 3.

4.1 Internal structure

We modelled the internal structure of LTT 9779 b assuming a silicate-iron (rocky) core surrounded by a large H/He-rich atmosphere, following [Rogers & Owen \(2021\)](#). This description entails a total of

³ The code is available on GitHub at <https://github.com/jorgefz/photoevolver>

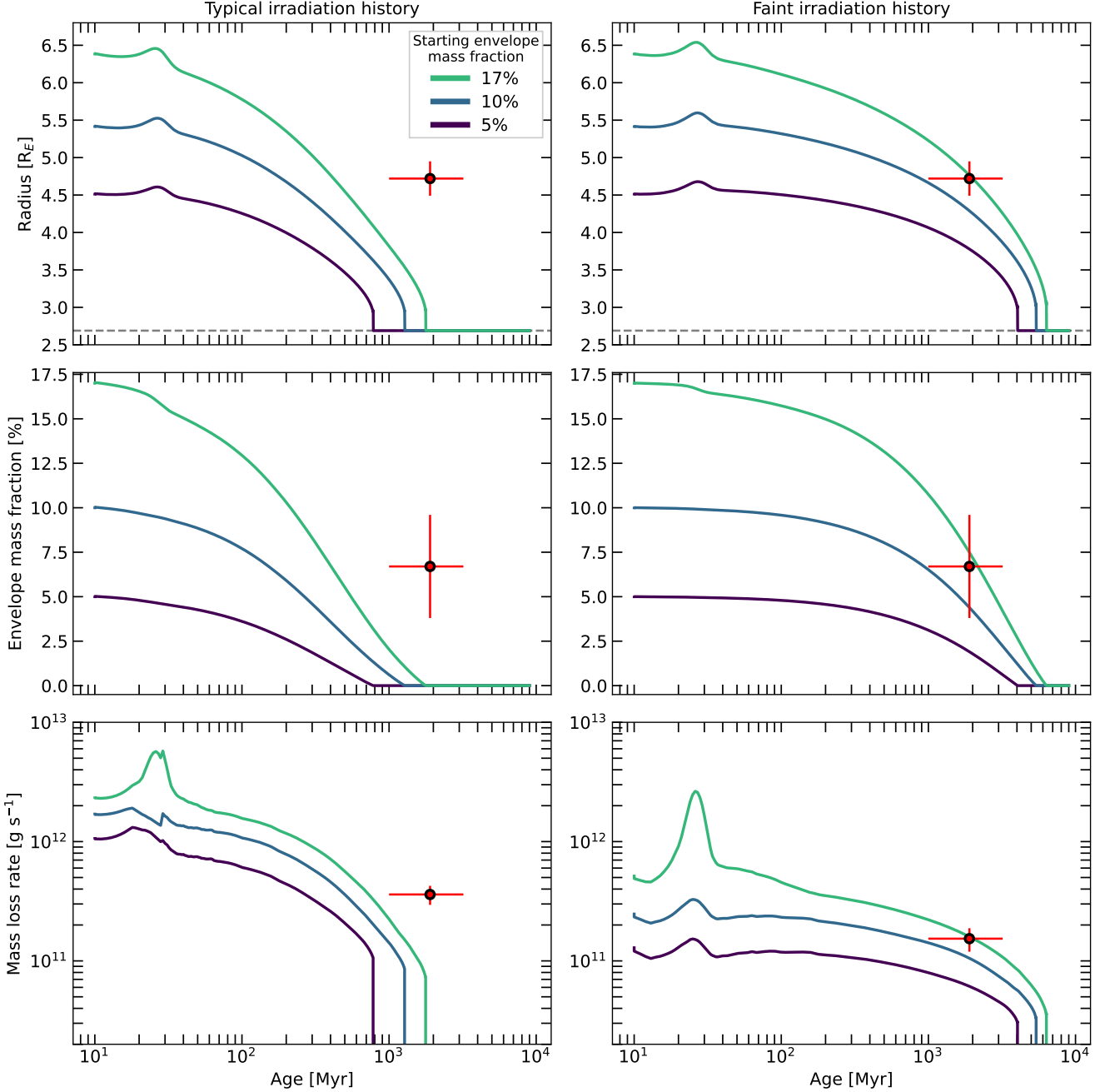


Figure 4. Evaporation histories of a range of simulated scenarios for LTT 9779 b, with initial envelope mass fractions from 5% to 17%. The panels present the evolution of the planet radius (top), envelope mass fraction (middle), and mass loss rate (bottom) under two XUV irradiation histories: (1) the expected stellar emission history of a solar mass star (left column), and (2) a fainter emission history consistent with the measured stellar rotation velocity and our X-ray upper limit from our *XMM-Newton* observation (right column). The dashed grey line on the top panels represents the rocky core radius of LTT 9779 b.

four model parameters: the core radius R_{core} , core mass M_{core} , envelope radius R_{env} , and envelope mass fraction f_{env} (see Table 4). With knowledge of the planet’s mass and radius alone (together with orbital and host star parameters), we can deduce values for these quantities by combining four equations. First we defined planet radius as $R_p = R_{\text{core}} + R_{\text{env}}$, and envelope mass fraction as the ratio of envelope and planet masses $f_{\text{env}} = M_{\text{env}}/M_p = (M_p - M_{\text{core}})/M_p$. Additionally, we adopted the empirical mass-radius relation for rocky planets by [Otegi et al. \(2020, Eqn. 1\)](#) to link the core mass M_{core} to

the core radius R_{core} . Finally, we adopt the envelope structure model by [Chen & Rogers \(2016, Eqn. 5\)](#), which links the mass fraction of the envelope f_{env} to its thickness R_{env} . We found that LTT 9779 b is consistent with a rocky core of radius $2.69 \pm 0.11 R_E$ and a gaseous envelope of mass fraction $6.7 \pm 2.9\%$ (see Table 4), in good agreement with the mass fraction of 9% estimated by [Jenkins et al. \(2020\)](#).

Moreover, we estimated that the predicted XUV emission for LTT 9779 induces a present-day mass loss rate of $3.5 \times 10^{11} \text{ g s}^{-1}$ using the model by [Kubyskhina et al. \(2018\)](#). Energy-limited photo-

Table 4. Planetary parameters and internal structure of LTT 9779 b.

Parameter		Value	Source
Orbital period	P_{orb} (days)	$0.792 \pm (9.3 \times 10^{-6})$	J20 ^a
Semi-major axis	a (AU)	0.01679 ± 0.00014	J20 ^a
Equilibrium temperature	T_{eq} (K)	1978 ± 19	J20 ^a
Mass	M_{p} (M_{E})	$29.30^{+0.78}_{-0.81}$	J20 ^a
Radius	R_{p} (R_{E})	4.72 ± 0.23	J20 ^a
Core radius	R_{core} (R_{E})	2.69 ± 0.11	This work
Core mass	M_{core} (M_{E})	27.30 ± 1.10	This work
Envelope radius	R_{env} (R_{E})	2.03 ± 0.26	This work
Envelope mass fraction	f_{env}	0.067 ± 0.029	This work

^a J20: Jenkins et al. (2020)

evaporation, a simpler model that accounts only for the energy from incident X-ray photons (Watson et al. 1981; Lecavelier Des Etangs 2007), predicts a lower present-day mass loss rate of $2.8 \times 10^{11} \text{ g s}^{-1}$ using the same evaporation efficiency as Kubyshkina et al. (2018) of 15%. On the other hand, the fainter XUV emission motivated by our *XMM-Newton* observations yields a present-day mass loss rate of $1.5 \times 10^{11} \text{ g s}^{-1}$ using the model by Kubyshkina et al. (2018), and $0.6 \times 10^{11} \text{ g s}^{-1}$ with the energy-limited formulation.

5 EVAPORATION HISTORY

We simulated a range of evolutionary scenarios for LTT 9779 b, all using the rocky core determined in Table 4, but each starting off at an age of 10 Myr with a different envelope mass fraction. We used envelope mass fractions of 5%, 10%, and 17%, with the lowest of these values being motivated by the uncertainty on the planet's current envelope mass fraction.

The maximum initial envelope is motivated by the maximum radius the planet could have following its formation. This is set by the radius of its Roche lobe which we calculate using the expression by Owen & Lai (2018, Eqn. 3) for low density gaseous planets. This gives a maximum envelope mass fraction of 17% for LTT 9779 b at the beginning of our simulation. Finally, the choice of initial envelope mass fraction of 10% serves as a mid-point between the two values above.

5.1 Expected XUV history

Firstly, we adopt the XUV luminosity tracks that are expected for a typical solar-mass star following the model by Johnstone et al. (2021), as shown in Figure 2 (right hand panel), and evolve LTT 9779 b under photoevaporation for the three initial envelope mass fractions. The results, shown in Figure 4 (left column) show that none of these scenarios match the mass and radius of LTT 9779 b at the present time, as they are all stripped of their envelopes before now. This confirms that a planet of this nature orbiting LTT 9779 with the expected X-ray emission history would already be a hot rocky world of radius $2.7 R_{\text{E}}$, joining the population of planets that define the lower edge of the Neptune desert. We thus rule out this scenario as a description of the evaporation history of LTT 9779 b.

5.2 Faint XUV history

We repeat the analysis in Sect. 5.1 but adopting a stellar XUV history that respects both the measured stellar rotation velocity and our X-ray upper limit, as determined with our *XMM-Newton* observation

(Sect. 2). This emission history, shown in Figure 2 (right hand panel), matches a star that has a rotation period of 45 days at the age of 2 Gyr.

We find that the planetary atmosphere survives evaporation to the present day for all three initial envelope fractions, as shown in Figure 4 (right column). Furthermore, we find that, under these conditions, LTT 9779 b is consistent with an evaporation history where it started out with an envelope mass fraction of 10% to 17%. This would make the planet a 6–7 R_{E} puffy super-Neptune after disc dispersal.

We find that continued exposure to these low XUV fluxes does end up stripping the planet of its envelope by the age of 6–7 Gyr (Figure 4). As can be seen in Figure 2, this is because the low activity track is flat in comparison to the high activity track, and so the X-ray emission in both histories become comparable at later ages. This behaviour can be attributed to faster rotators spinning down more rapidly than slow rotators, leading to the tracks converging (Johnstone et al. 2021).

In principle, our conclusion that the low activity track is consistent with the planet retaining its envelope to the present day is sensitive to our choice of EUV scaling law. This is illustrated in Fig. 3, where it is clear that the EUV emission is expected to be higher than X-rays throughout the lifetime of the star. Maggio et al. (2023) compared different X-ray/EUV scaling laws and confirmed that the King et al. (2018) relation used here is in good agreement with available EUV observations. Some other EUV scaling laws, however, such as that from Sanz-Forcada et al. (2011) predict somewhat higher EUV emission up to a factor 2 (revised down to 1.5 by Sanz-Forcada et al. 2022). In order to test whether the choice of scaling relation affects our conclusions, we re-ran our model with both the Sanz-Forcada et al. (2011) and Sanz-Forcada et al. (2022) relations. We found that the gaseous envelope of the planet is still expected survive to the present day for both scaling relations, demonstrating that our results in practice are not sensitive to this choice.

6 DISCUSSION & CONCLUSIONS

We have presented an analysis of X-ray driven photoevaporation of the ultra-short period Neptune LTT 9779 b: the only known planet deep in the Neptune desert with a significant gaseous envelope. Since the Neptune desert is thought to be cleared out by X-ray photoevaporation (e.g. Owen & Lai 2018), the existence of this planet at such a short period is puzzling.

Specifically, we have considered the possibility that LTT 9779 b has survived at its present orbital separation due to anomalously low X-ray emission from its host star, as suggested by its unusually low rotational velocity (Table 1) and lack of Ca II HK emission lines (Jenkins et al. 2020).

We made an *XMM-Newton* observation of the host star and measured an upper-limit to the X-ray luminosity that is a factor of fifteen lower than the expected X-ray luminosity for a star of this type and age (Sects. 2 & 3). In contrast, our X-ray upper limit is within a factor of 2 of the luminosity expected for a star rotating with the much slower 45 d period suggested by the rotational velocity and an assumed alignment between the stellar spin and planetary orbital axes.

We also simulated the possible evaporation history of the planet using a range of initial envelope mass fractions. As expected, we confirm that the planetary atmosphere would not survive to the present day under the expected X-ray emission history of a solar mass star like LTT 9779 (Sect. 5.1). However, we find that a dimmer X-ray past, motivated by the upper limits on the X-ray luminosity and spin period, allows the planetary atmosphere to survive to the present day (Sect. 5.2).

We conclude that LTT 9779 most-likely formed as an anomalously slowly rotating star, and that its close-in Neptune-sized planet LTT 9779 b was thus able to survive in the Neptune desert to the present day due to unusually low X-ray irradiation. This scenario is consistent with the planet forming in situ and/or migrating within the protoplanetary disc, offering an alternative to the scenario suggested by Jenkins et al. (2020), in which late inward migration followed by Roche-lobe overflow (RLO) may have eroded a Jupiter-mass planet down to a hot Neptune like LTT 9779 b.

Moreover, the super-solar (400×) metallicity of its atmosphere together with its very high albedo, determined by Hoyer et al. (2023), would make the planet more resistant to evaporation as heavier species require more energy to remove (Wilson et al. 2022; Owen & Jackson 2012).

Even though the implied slow 45-day spin of LTT 9779 may be unusual, examples of long-period (30–45 d) solar-mass stars have been found in the 950 Myr-old cluster NGC 6811, hinting towards a rare mechanism that yields extremely slow rotators (Godoy-Rivera et al. 2021).

This unusual feature of the host star is consistent with our interpretation because of the unique nature of LTT 9779 b within the Neptunian desert. The strong selection bias in favour of large close-in transiting exoplanets means that planets like LTT 9779 b must be extremely rare. In contrast, finding similarly anomalous stars without a hot Neptune is extremely difficult. This is because their low stellar activity results in low amplitude photometric modulation that is difficult to detect. Their long periods are also beyond the reach of most photometric surveys, and we cannot use $v \sin i$ because of contamination by pole-on faster rotators. Nevertheless, it is known that stars are formed with a wide range of initial spin periods, at least in part due to interactions with long-lived protoplanetary discs (~10 Myr), which can prevent them from spinning-up during the pre-main sequence stage of their evolution and allowing slow rotators to maintain their initial spin into the main sequence (e.g. Moraux et al. 2013; Ribas et al. 2015; Richert et al. 2018).

Finally, our conclusion that the only known planet deep in the Neptunian desert with a gaseous envelope is also unusual in having an X-ray faint star, strongly supports the suggestion that the primary origin of the Neptunian desert is X-ray driven photoevaporation.

ACKNOWLEDGEMENTS

The work presented here was supported by the UK Science and Technology Facilities (STFC). JFF is supported by the STFC studentship grant ST/W507908/1. PW acknowledges support under the STFC consolidated grants ST/T000406/1 and ST/X001121/1. JSJ gratefully acknowledges support by FONDECYT grant 1201371 and from the ANID BASAL project FB210003. This research made use of the Python packages `numpy` (Harris et al. 2020), `astropy` (Astropy Collaboration et al. 2022), `scipy` (Virtanen et al. 2020), `matplotlib` (Hunter 2007), `Mors` (Johnstone et al. 2021), and `uncertainties`⁴. This research has made use of the NASA Exoplanet Archive, which is operated by the California Institute of Technology, under contract with the National Aeronautics and Space Administration under the Exoplanet Exploration Program. Based on observations obtained with XMM-Newton, an ESA science mission with instruments and contributions directly funded by ESA Member States and NASA.

We thank the reviewer for their constructive comments which have improved the quality of this work.

DATA AVAILABILITY

The XMM-Newton data used in this work is publicly available at the XMM-Newton Science Archive (XSA)⁵, under the observation ID 0884250101 (target: LTT 9779, PI: Wheatley).

REFERENCES

- Armstrong D. J., et al., 2020, *Nature*, **583**, 39
- Arnaud K. A., 1996, in Jacoby G. H., Barnes J., eds, *Astronomical Society of the Pacific Conference Series Vol. 101, Astronomical Data Analysis Software and Systems V*. p. 17
- Asplund M., Grevesse N., Sauval A. J., Scott P., 2009, *ARA&A*, **47**, 481
- Astropy Collaboration et al., 2022, *apj*, **935**, 167
- Benítez-Llambay P., Masset F., Beaugé C., 2011, *A&A*, **528**, A2
- Borucki W. J., et al., 2011, *ApJ*, **736**, 19
- Chen H., Rogers L. A., 2016, *ApJ*, **831**, 180
- Christiansen J. L., et al., 2022, *AJ*, **163**, 244
- Cloutier R., Charbonneau D., Deming D., Bonfils X., Astudillo-Defru N., 2021, *AJ*, **162**, 174
- Crossfield I. J. M., et al., 2020, *ApJ*, **903**, L7
- Cutri R. M., et al., 2003, *VizieR Online Data Catalog*, p. II/246
- Dragomir D., et al., 2020, *ApJ*, **903**, L6
- Edwards B., et al., 2023, *arXiv e-prints*, p. arXiv:2306.13645
- Farihi J., et al., 2018, *MNRAS*, **474**, 947
- Fedele D., van den Ancker M. E., Henning T., Jayawardhana R., Oliveira J. M., 2010, *A&A*, **510**, A72
- Fernández Fernández J., Wheatley P. J., King G. W., 2023, *MNRAS*, **522**, 4251
- Fulton B. J., et al., 2017, *AJ*, **154**, 109
- Gaia Collaboration et al., 2022, *arXiv e-prints*, p. arXiv:2208.00211
- Godoy-Rivera D., Pinsonneault M. H., Rebull L. M., 2021, *ApJS*, **257**, 46
- Güdel M., 2004, *A&ARv*, **12**, 71
- Harris C. R., et al., 2020, *Nature*, **585**, 357
- Hoyer S., et al., 2023, *A&A*, **675**, A81
- Hunter J. D., 2007, *Computing in Science & Engineering*, **9**, 90
- Ionov D. E., Pavlyuchenkov Y. N., Shematovich V. I., 2018, *MNRAS*, **476**, 5639
- Jackson B., Arras P., Penev K., Peacock S., Marchant P., 2017, *ApJ*, **835**, 145
- Jenkins J. S., et al., 2020, *Nature Astronomy*, **4**, 1148
- Johnstone C. P., Bartel M., Güdel M., 2021, *A&A*, **649**, A96
- King G. W., et al., 2018, *MNRAS*, **478**, 1193
- Koskinen T. T., Lavvas P., Huang C., Bergsten G., Fernandes R. B., Young M. E., 2022, *ApJ*, **929**, 52
- Kraft R. P., Burrows D. N., Nousek J. A., 1991, *ApJ*, **374**, 344
- Kubyskhina D., et al., 2018, *ApJ*, **866**, L18
- Kurokawa H., Kaltenecker L., 2013, *MNRAS*, **433**, 3239
- Kurokawa H., Nakamoto T., 2014, *ApJ*, **783**, 54
- Lammer H., et al., 2016, *MNRAS*, **461**, L62
- Lecavelier Des Etangs A., 2007, *A&A*, **461**, 1185
- Lopez E. D., Fortney J. J., 2014, *ApJ*, **792**, 1
- Lopez E. D., Fortney J. J., Miller N., 2012, *ApJ*, **761**, 59
- Maggio A., et al., 2023, *ApJ*, **951**, 18
- Matsakos T., Königl A., 2016, *ApJ*, **820**, L8
- Mazeh T., Holczer T., Faigler S., 2016, *A&A*, **589**, A75
- Moraux E., et al., 2013, *A&A*, **560**, A13
- Murray-Clay R. A., Chiang E. I., Murray N., 2009, *ApJ*, **693**, 23
- Osborn A., et al., 2023, *MNRAS*,
- Otegi J. F., Bouchy F., Helled R., 2020, *A&A*, **634**, A43

⁴ Uncertainties: a Python package for calculations with uncertainties, Eric O. Lebigot, <http://pythonhosted.org/uncertainties>

⁵ <https://www.cosmos.esa.int/web/xmm-newton/xsa>

- Owen J. E., Jackson A. P., 2012, *MNRAS*, **425**, 2931
- Owen J. E., Lai D., 2018, *MNRAS*, **479**, 5012
- Owen J. E., Wu Y., 2013, *ApJ*, **775**, 105
- Owen J. E., Wu Y., 2016, *ApJ*, **817**, 107
- Owen J. E., Wu Y., 2017, *ApJ*, **847**, 29
- Pizzolato N., Maggio A., Micela G., Sciortino S., Ventura P., 2003, *A&A*, **397**, 147
- Redfield S., Linsky J. L., 2001, *ApJ*, **551**, 413
- Ribas Á., Bouy H., Merín B., 2015, *A&A*, **576**, A52
- Richert A. J. W., Getman K. V., Feigelson E. D., Kuhn M. A., Broos P. S., Povich M. S., Bate M. R., Garmire G. P., 2018, *MNRAS*, **477**, 5191
- Rodríguez J. E., et al., 2018, *AJ*, **156**, 245
- Rogers J. G., Owen J. E., 2021, *MNRAS*, **503**, 1526
- Sanchis-Ojeda R., Rappaport S., Winn J. N., Kotson M. C., Levine A., El Mellah I., 2014, *ApJ*, **787**, 47
- Sanz-Forcada J., Micela G., Ribas I., Pollock A. M. T., Eiroa C., Velasco A., Solano E., García-Álvarez D., 2011, *A&A*, **532**, A6
- Sanz-Forcada J., López-Puertas M., Nortmann L., Lampón M., 2022, in Cambridge Workshop on Cool Stars, Stellar Systems, and the Sun. Cambridge Workshop on Cool Stars, Stellar Systems, and the Sun. p. 138, [doi:10.5281/zenodo.7561725](https://doi.org/10.5281/zenodo.7561725)
- Smith R. K., Brickhouse N. S., Liedahl D. A., Raymond J. C., 2001, *ApJ*, **556**, L91
- Strüder L., et al., 2001, *A&A*, **365**, L18
- Szabó G. M., Kiss L. L., 2011, *ApJ*, **727**, L44
- Turner M. J. L., et al., 2001, *A&A*, **365**, L27
- Virtanen P., et al., 2020, *Nature Methods*, **17**, 261
- Vissapragada S., et al., 2022, *AJ*, **164**, 234
- Watson A. J., Donahue T. M., Walker J. C. G., 1981, *Icarus*, **48**, 150
- West R. G., et al., 2019, *MNRAS*, **486**, 5094
- Wilms J., Allen A., McCray R., 2000, *ApJ*, **542**, 914
- Wilson T. G., et al., 2022, *MNRAS*, **511**, 1043
- Wright N. J., Drake J. J., Mamajek E. E., Henry G. W., 2011, *ApJ*, **743**, 48
- Wright N. J., Newton E. R., Williams P. K. G., Drake J. J., Yadav R. K., 2018, *MNRAS*, **479**, 2351
- Yelle R. V., 2004, *Icarus*, **170**, 167
- Zacharias N., Finch C. T., Girard T. M., Henden A., Bartlett J. L., Monet D. G., Zacharias M. I., 2012, VizieR Online Data Catalog, p. [I/322A](https://vizier.cesr-bcm.fr/vizieR/1322A)

This paper has been typeset from a $\text{\TeX}/\text{\LaTeX}$ file prepared by the author.